Title
Engineering CoO x –Based Self-Supported Anodes for Pure-Water-Fed Anion-Exchange-Membrane Electrolysis

Journal
ACS Catalysis, 16(1)

ISSN
2155-5435

Authors
Kwak, Minkyoung
Hou, Shujin
Spence, Kieran J
et al.

Publication Date
2026-01-02

DOI
10.1021/acscatal.5c05942

Engineering CoO_x-Based Self-Supported Anodes for Pure-Water-Fed Anion-Exchange-Membrane Electrolysis

Minkyoung Kwak[1,2,3], Shujin Hou[2,3], Kieran J. Spence[4], Tekalign T. Debela[1,5] and Shannon W. Boettcher[1,2,3]*

[1]*Oregon Center for Electrochemistry, Department of Chemistry and Biochemistry, University of Oregon, Eugene, OR 97403, United States*
[2]*Departments of Chemical & Biomolecular Engineering and Chemistry, University of California, Berkeley, CA 94720, United States*
[3]*Energy Storage and Distributed Resources Division, Lawrence Berkeley National Laboratory, Berkeley, CA 94720, United States*
[4]*De Nora Tech, LLC, Concord, OH 44077, United States*
[5]*Department of Chemistry and Physical Science, Methodist University, Fayetteville, NC 28311, United States*

*Corresponding Author: boettcher@berkeley.edu

Abstract: Commercial membrane electrolyzers rely on acidic fluorocarbon membranes and ionomers, requiring the use of expensive IrO_x-based oxygen-evolution catalysts. Anion-exchange-membrane water electrolyzers (AEMWEs) operate in an alkaline environment, enabling the use of non-precious-metal catalysts. Here, we study and engineer CoO_x-based catalyst-coated anodes deposited via hydrothermal synthesis directly onto porous transport layers both with and without thermal annealing. Self-supported, nanoneedle-structured Co_3O_4 anode, formed by annealing the as-synthesized cobalt carbonate hydroxide, $Co(CO_3)_x(OH)_y$, outperforms the baseline Co_3O_4 nanoparticle ink-based anode in pure-water-fed AEMWE, due to improved catalyst layer continuity and thus number of electroactive Co species. The as-synthesized and unannealed $Co(CO_3)_x(OH)_y$), however, appears to undergo substantial conversion to a more-active $CoO_x(OH)_y$ phase predominantly at the surface, with nominally Co^{3+} present and higher electrical conductivity, lowering the cell voltage ~200 mV at 1.0 $A{\cdot}cm^{-2}$ in pure-water-fed AEMWE compared to the conventional Co_3O_4 nanoparticle anodes. We analyze the differences in electrode electrochemical response between pure-water and KOH feed modes finding distinct activation and degradation modes. The $Co(CO_3)_x(OH)_y$ anode shows significant activation and slower degradation linked to

the conversion to oxyhydroxide. We propose catalyst layer designs that promote both hydroxide and electron transport, alongside interfacial engineering strategies to obtain high performance while mitigating anode degradation.

Keywords: anion-exchange-membrane water electrolysis, self-supported catalyst, catalyst-ionomer interface, non-precious-group-metal catalyst, oxygen evolution reaction

Introduction

Anion-exchange-membrane water electrolysis (AEMWE) is an emerging technology for H_2 production.[1] In principle, AEMWE combines advantages from proton-exchange-membrane water electrolyzers (PEMWE)—low resistance, zero-gap membrane-electrode assemblies, and dynamic, pure-water operation—and those of liquid alkaline water electrolyzers (AWE) that use of inexpensive materials for catalysts and flow fields. However, AEMWE technology is limited by difficulty in designing high-performance electrodes and their poor durability, in large part from ionomer/membrane instability.[2] Ionomers incorporated in anodes are oxidized during operation, limiting hydroxide transport, and this process is accelerated when the anodes are fed with pure water.[3-5]

In PEMWE, IrO_x-based catalysts have good performance and stability for the oxygen-evolution reaction (OER), and are the only materials used in commercial PEMWE devices.[6-8] IrO_x catalyst nanoparticle inks are prepared with mixtures of ionomer and solvent solutions from which the anode porous-electrode layer is fabricated. This ink-based approach works in part because IrO_x has high electrical conductivity ($\sim 10^4$ $S \cdot cm^{-1}$)[9] so that the electrical resistance of the particle network is sufficiently low despite being mixed with ionomer which reduces particle-particle contacts. Ir is scarce and expensive, though, which limits the scalability of PEM water electrolyzers.[10] AEMWE can use non-precious group metals (non-PGMs) owing to the alkaline environment where many metal oxides are (largely) insoluble.[1, 11] Non-PGM anodes in AEMWE devices also outperform Ir-based anodes[4, 12] as IrO_2 has moderate OER activity in alkaline conditions.[4, 12, 13] One issue is that non-PGM catalysts, such as those based on Co or Ni oxides, are

semiconducting and thus have insufficient electrical conductivity to build optimal porous electrodes using ink processing.

Engineering electrode geometry beyond the typical random assemblies of nanoparticles and ionomer from inks can be used to improve electron, ion, and gas transport pathways through the catalyst-ionomer network. Conventionally, catalyst nanoparticles are mixed with ionomers, sometimes with additional binders or conductive non-catalytic supports, in water-alcohol mixed solvents with an optimized catalyst-to-ionomer ratio. These ink solutions are coated by spraying or other means onto porous transport layers (PTLs) or membranes.[3, 14] This approach is useful from a manufacturing perspective,[14, 15] however, due to structural complexity, controlling or identifying the dominant conduction pathways remains challenging,[16, 17] and this complexity prevents a clear assessment of whether alternative architectures can achieve substantially superior performance.[14] Ionomers partially cover the catalyst particles, increasing interparticle electrical resistance and lowering electric conductivity within the catalyst layer **(Scheme 1**, left).[16-18]. Ionomer and/or binder incorporated in anode catalyst layers can also be oxidized during operation, affecting durability.[4, 5, 16, 17, 19]

Self-supported electrodes, where inorganic catalysts are deposited as continuous layers directly on the PTLs, enable engineering the electron-conduction pathways, and the adhesive bonding properties of ionomers between inorganic nanoparticles are unneeded (**Scheme 1**, right). Nano-structuring, in principle, can also be judicially controlled to enhance electroactive surface area, increase catalyst loading, and control surface wetting and bubble removal. These attributes are all useful for robust, high-current-density operation.[16, 20] Nanostructured electrode fabrication, however, with such desired properties is nontrivial, especially in manufacturing.

KOH-fed AEMWE cells have been demonstrated with self-supported anodes, mostly using NiFe-oxy(hydroxide)-based OER catalysts.[21-23] The addition of soluble KOH simplifies electrode design because the liquid electrolyte permeates pores of all sizes in the solid and maximizes catalyst utilization across the entire PTL-supported layer, which is not possible with a solid-ionomer electrolyte using pure-water feed that is ultimately desired for AEMWE.[24] It is further challenging to adopt NiFe-based, and related, self-supported catalysts in pure-water systems because of their poor electrical conductivity when they are not transformed to the more-conductive oxyhydroxide forms due to limited OH^- accessibility,[25] as well as due to durability concerns arising from Fe leaching.[26] Further, the recently developed passivated electrode architecture[27]

extends electrode lifetime and integrates naturally with self-supported catalysts due to well-defined catalyst-ionomer interface available to coat prior to ionomer infiltration. This is particularly important as no known ionomers remain stable in the alkaline and oxidizing environment of the AEMWE anode,[5] highlighting the need to understand and advance self-supported electrode designs.

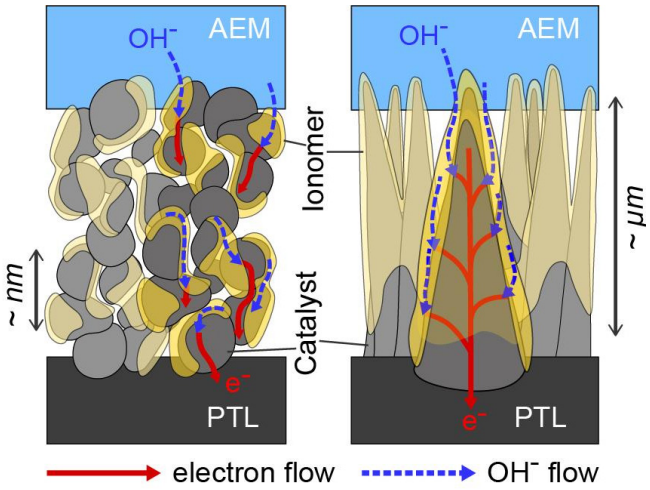

Scheme 1. Comparison of electrode geometry between NP ink-based (left) vs. self-supported (right) anodes. The electronic and ionic pathways are affected by the electrode microstructures forming triple-phase boundaries. The NP ink-based anode possesses regions of disconnected nanoparticles and regions without ionomers covering the surface, while the self-supported anode schematic emphasizes the controllability of micro- and nanoscale electronic and ionic conduction pathways.

Here, Co-based anodes were grown directly on PTLs using a hydrothermal synthesis with controlled materials phase and nanostructure to study the link between electrode response, materials properties, and nanostructure. The resulting PTL-supported $Co(CO_3)_x(OH)_y$ and Co_3O_4 anodes were evaluated in pure-water-fed AEMWE devices and compared to conventional nanoparticle ink-based anodes. By controlling the growth, we show improved performance of self-supported $Co(CO_3)_x(OH)_y$ associated with abundance of electroactive Co species and improved catalyst layer continuity. The $Co(CO_3)_x(OH)_y$ catalyst layer transformed, partially, into a mixed $CoO_x(OH)_y$ phase (Co^{2+}/Co^{3+}) during the cell activation, providing lower cell voltages at higher current densities compared to the annealed Co_3O_4 anode. Electrode capacitance measurements during cell activation and continuous operation, however, show that the catalyst-ionomer interfaces degrade under pure-water feed compared to KOH feed. This challenge may be resolved with interfacial engineering strategies building onto self-supported electrodes.

Results and Discussion

Fabrication of Co-based Self-supported Anodes. We deposited nanostructured Co-based OER catalysts on PTLs using a modified hydrothermal synthesis.[28-30] Cobalt nitrate salt and urea were dissolved in deionized water with a Ni-alloy PTL substrate submerged in the solution (Figures S1 and S2). Upon heating to 100 °C, urea decomposed and hydrolyzed, releasing carbonate and hydroxide ions[31] that raise the pH and induce the growth of cobalt carbonate hydroxide (nominally $Co(CO_3)_x(OH)_y$) on the PTL (**Figure 1a**). The $Co(CO_3)_x(OH)_y$ grown PTL was used directly as the OER pre-catalyst or converted to its oxide form via calcination prior to electrochemical testing, while excess material precipitated at the bottom of the vessel was washed with DI water, centrifuged, and reserved as a powder for characterization.

The morphology and loading of the synthesized $Co(CO_3)_x(OH)_y$ were controlled by modifying hydrothermal reaction times and conditions (see SI). Powder X-ray diffraction (PXRD) analysis of the precipitates before and after annealing shows a phase transformation from $Co_6(CO_3)_2(OH)_8 \cdot H_2O$ with a weak α-$Co(OH)_2$ (003) reflection, noted as *, to spinel-phase Co_3O_4 after annealing at 300 °C for 2 h in air (**Figure 1b**). We note that PXRD is not sensitive to poorly crystalline or amorphous components which may also be present particularly in the as-synthesized materials. Co 2p X-ray photoelectron spectrum (XPS) shows a shift from predominantly Co^{2+} to a mixed Co^{2+}/Co^{3+} state after annealing, as indicated by changes in the binding energy of the main and satellite peaks (Co^{2+} at ~781–782 eV; Co^{3+} at 779.9 eV for main $2p_{3/2}$ peaks; Co^{2+} at ~785–786 eV; Co^{3+} at 789.8 eV for $2p_{3/2}$ satellite peaks, respectively, summarized in Table S1) and consistent with this phase transformation (**Figure 1c**).[32, 33] The lattice oxygen peak at ~530 eV in O 1s XP spectra sharpens upon oxide formation after annealing, while the feature at ~532 eV associated with carbonate species and adsorbed water molecules is reduced in intensity.[34] Scanning electron microscopy (SEM) images (**Figure 1d**) show a nanoneedle-structured Co_3O_4 on the Ni alloy PTL, synthesized using the optimized hydrothermal synthesis. The cross-sectional SEM image obtained after focused-ion-beam (FIB) milling shows a ~5 μm thick catalyst on the PTL.

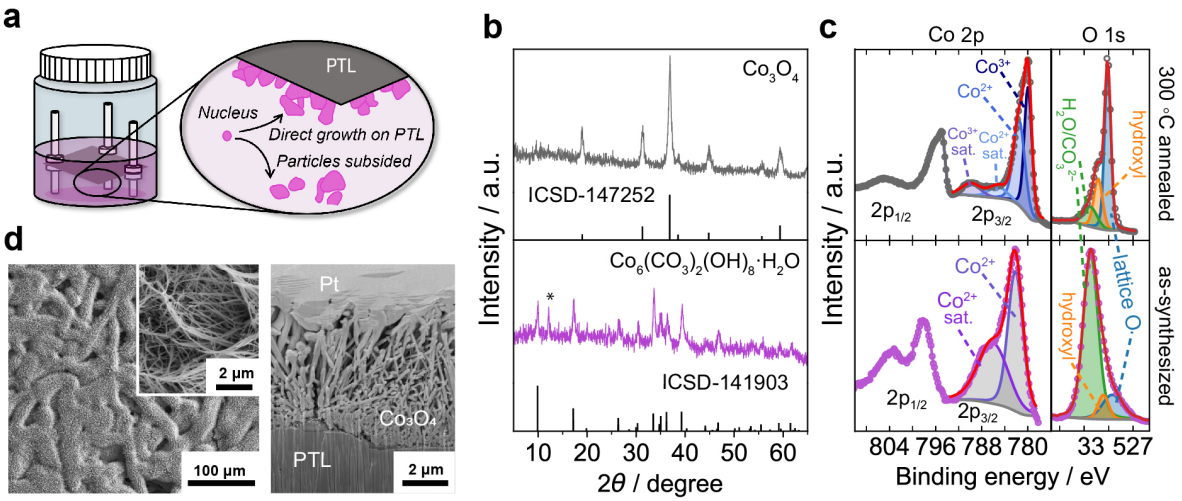

Figure 1. (a) Hydrothermal synthesis schematic. The catalysts were deposited directly on the PTL, with some additional solution-phase growth as precipitates. (b) Powder X-ray diffraction patterns of powders as synthesized and after 300 °C annealing match $Co_6(CO_3)_2(OH)_8 \cdot H_2O$ and Co_3O_4, respectively. A minor peak (*) is attributed to α-$Co(OH)_2$ impurities. (c) XP spectra of catalysts as synthesized and after 300 °C annealing on Ni alloy PTL. After annealing, as-synthesized $Co(CO_3)_x(OH)_y$ transformed to Co_3O_4. (d) SEM top-down and cross-sectional images of prepared Co_3O_4 deposited on Ni alloy PTL showing nanoneedle structure of Co_3O_4 deposited on PTL. A Pt layer was deposited on the sample to protect it during cross-sectioning. SEM images were obtained after annealing to form Co_3O_4 because the $Co(CO_3)_x(OH)_y$ samples exhibited charging-related imaging artefacts due to their non-conductive nature. No significant morphological differences were observed between the Co_3O_4 and $Co(CO_3)_x(OH)_y$ samples on the length scales observed in the SEM.

Effect of Electrode Microstructure. Baseline NP-based Co_3O_4 anodes were prepared by mixing Co_3O_4 NPs with PiperION (PAP-TP-85) ionomer in isopropyl alcohol and deionized water, followed by sonication and spray-coating on Ni alloy PTLs (1.7 $mg \cdot cm^{-2}$).[3] For comparison, the self-supported annealed Co_3O_4 catalyst layer on the Ni alloy PTL was prepared with a loading of 1.5 $mg \cdot cm^{-2}$ (optimization details from the hydrothermal synthesis are provided in the Supporting Information; Figures S3 and S4). We incorporate ionomer (PiperION TP-85) onto the self-supported Co_3O_4 anode by dip-coating (ionomer loading of 1.0 ± 0.2 $mg \cdot cm^{-2}$), as well as onto the bare Ni-alloy PTL as a control sample.[27, 35] SEM images in Figure S5 confirmed uniform ionomer coverage. All anodes were assembled in AEMWE devices with NP-based Pt-black cathodes (2.0

mg·cm^{-2}) and a 40-μm PiperION membrane and tested at 56 ± 1 °C with pure-water feed following the procedures detailed in Methods section.

Polarization curves (**Figure 2a**) for AEMWE cells with self-supported Co_3O_4, Co_3O_4 NPs, and bare Ni alloy PTL anodes show that the self-supported Co_3O_4 anode exhibits lower cell voltages at 1.0 A·cm^{-2} than the NP ink-based anode by ~120 mV, and by ~190 mV compared to the bare Ni alloy anode. Electrochemical impedance spectroscopy (EIS) data at 50 mA·cm^{-2} (**Figure 2b**) also indicate a lower high frequency resistance (HFR) for the self-supported anode compared to the ink-based anode and bare Ni alloy anode (0.120, 0.156, and 0.130 Ω·cm^2, respectively). Although the HFR does not fully capture mixed ionic/electronic resistances in the porous electrode due to the parallel equivalent capacitance,[36, 37] the lower resistance suggests better electrical interconnection between the catalyst layer and PTL in the self-supported Co_3O_4. The higher catalytic activity of the self-supported Co_3O_4 anode is also from a lower charge-transfer resistance, R_{CT}, than the NP-ink based anode (1.08 Ω·cm^2 vs. 1.28 Ω·cm^2). Details of the EIS data analysis and fitting results are provided in the Supporting Information. The improved R_{CT} in EIS is consistent with lower *iR*-corrected overpotential observed vs. current density (Figure S8) for the self-supported Co_3O_4 anode, indicating that this architecture not only reduces the catalyst-layer resistance but also enhances apparent OER kinetics. It is worth noting that, unlike in the self-supported anode, an excessive ionomer topcoat (~ 1.0 mg·cm^2) on NP-based anodes is not beneficial, as the thick ionomer coating appears to hinder both electronic and ionic transport to the anode catalyst, lowering its effectiveness (Figure S9).

Cyclic voltammograms (CVs) in **Figure 2c** compare (pseudo)capacitive currents of the prepared anodes from 0.6 to 1.0 V in a two-electrode configuration. At 1.0 V, the self-supported anode exhibits approximately four times higher capacitive currents than the ink-based anode. The bare Ni-alloy PTL anode, included as a control, shows minimal capacitive current as expected, in the absence of active catalyst material. The (pseudo)capacitive voltammogram shapes also differ. The self-supported anode shows substantial capacitive current across the entire voltage window, with a roughly linear capacitance increase as the voltage was scanned positively. In contrast, the nanoparticle anode shows current only on the positive sweep at voltages above 0.6 V, with a less-square charging-box shape at the positive-voltage limit. These observations indicate resistive limitations in accessing the bulk of the porous electrode for nanoparticles, compared to the self-supported catalysts.

The electronic properties of the Co_3O_4 under electrochemical conditions are complex, as Co_3O_4 is a semiconductor with relatively low electronic conductivity.[38] Its surface is redox-active, likely forming cobalt oxyhydroxide and related phases under OER conditions. Cobalt (oxy)hydroxides are insulators as Co^{2+} but electrically conductive when oxidized to predominantly Co^{3+}.[39] The onset of substantial capacitive current at 0.8 to 1.0 V likely corresponds to the oxidation of surface Co species, reducing interparticle resistances. The absence of this onset along with the higher (pseudo)capacitive current in the self-supported Co_3O_4, are consistent with improved electrical conductivity in the ionomer/catalyst porous electrode and a higher number of electronically and ionically accessible Co-based active sites for the self-supported sample.

The interpretation of the AEMWE device metrics and responses are consistent with the cross-sectional images in **Figure 2d-e**. In the nanoparticle Co_3O_4 anode, we observed inter-particle disconnections (limiting electron transport) as well as catalyst regions without ionomer coverage (limiting ion transport). In contrast, the self-supported Co_3O_4 show micron-length nanoneedles, with ionomers covering most of the catalyst surface–structures, as represented schematically in **Scheme 1**.

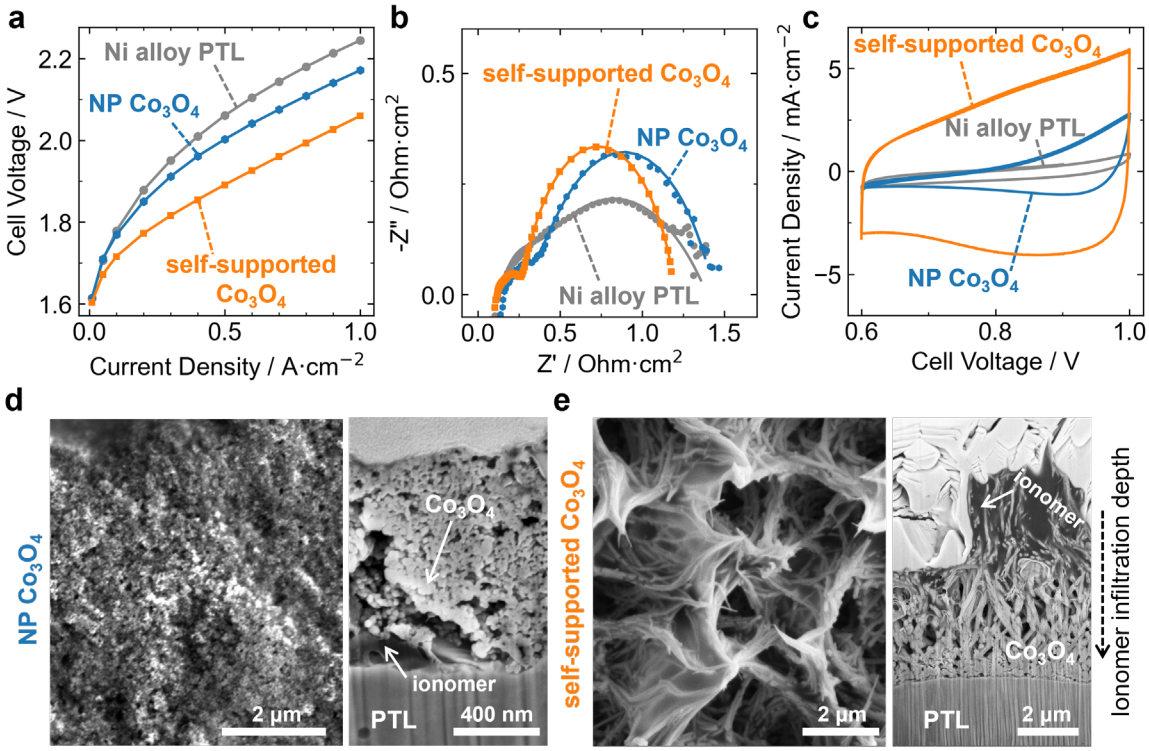

Figure 2. (a) Polarization curves of pure-water-fed AEMWE cells at 56 °C with self-supported Co_3O_4 on PTL, NP ink-based Co_3O_4 on PTL, and bare Ni alloy PTL. (b) EIS Nyquist plots at a current

density of 50 mA·cm^{-2} and (c) two-electrode cyclic voltammograms at a scan rate of 100 mV·s^{-1} for AEMWE cells with different anodes. Top-view and cross-sectional SEM images of (d) NP Co_3O_4 anode and (e) self-supported Co_3O_4.

Activation and Degradation of $Co(CO_3)_x(OH)_y$ and Co_3O_4 Anodes. The phase of OER catalysts and their corresponding electrical conductivities affect the AEMWE cell activation and durability because they govern both the catalyst layer resistance[40] and surface reconstruction/activation of Co-based catalyst to the oxyhydroxide form.[41, 42] Here, we compared self-supported $Co(CO_3)_x(OH)_y$ and Co_3O_4 coated anodes, each with 1.0 mg·cm^{-2} of PiperION topcoat in an AEMWE device. The $Co(CO_3)_x(OH)_y$ pre-catalyst exhibits better performance than the Co_3O_4, with a 90 mV lower cell voltage at 1.0 A·cm^{-2} (**Figure 3a**). The *iR*-corrected overpotential vs. current-density plots (**Figure 3b)** show that while the Tafel slopes of $Co(CO_3)_x(OH)_y$ and Co_3O_4 are similar, $Co(CO_3)_x(OH)_y$ achieves a higher current density at the same overpotential across the entire range. For example, at an overpotential of η = 300 mV, $Co(CO_3)_x(OH)_y$ reaches 6.3 mA·cm^{-2} compared to 2.1 mA·cm^{-2} for Co_3O_4. At higher current densities > 0.3 A·cm^{-2} (marked as red in the plot), the Co_3O_4 sample shows greater residual overpotentials, likely due to higher ionic and/or electronic resistance within catalyst layer affecting catalyst utilization. Some contribution to the residual overpotential may arise from mass-transport limitation of water or product gas in the porous electrode, although this effect is probably largely misassigned to the residual overpotential in many electrolyzer studies.[40, 43]

Typically, a freshly assembled AEMWE cell starts with a break-in step involving either a constant current hold for extended time or a series of constant current holds stepping up to the final current density.[3, 44] This initial procedure allows for catalyst reconstruction, membrane and ionomer hydration, and stabilization of the interfacial contacts, thereby providing more-reliable steady-state voltage measurements.[3, 44] In this work, all polarization curves were obtained after the current was stepped up to 1.0 A·cm^{-2} to ensure sufficient anode catalyst activation and voltage stabilization. However, for the following experiments (Figure 3c and Figure S8) aimed to investigate the activation behavior of $Co(CO3)_x(OH)_y$ pre-catalyst and Co_3O_4, an alternative procedure was designed and conducted on a different set of freshly assembled AEMWE cells: 50 cycles of CV were performed, followed by a chronopotentiometry (CP) step holding the current density at 0.5 A·cm^{-2} for 10 min (Figure S11a), and these CV-CP steps were repeated 20 times in a loop. The CV scans were used to monitor the evolution of (pseudo)capacitive current (see Figure

S10 for detailed implications underlying CV analysis), reflecting changes in the number of electrochemically active sites for a given sample, while the CP steps activate the catalyst surface under oxidative potential analogous to a conventional break-in process.

Figure 3c shows the initial CVs up to the third loop in the above process. The self-supported $Co(CO_3)_x(OH)_y$ shows a progressive increase of capacitive currents upon each CP step, indicating continuous activation to active surface oxyhydroxide, while Co_3O_4 shows a steady decrease. This suggests that $Co(CO_3)_x(OH)_y$ undergoes greater surface reconstruction into the conductive and active $CoO_x(OH)_y$ compared to Co_3O_4. This finding is interesting given that the $Co(CO_3)_x(OH)_y$ exhibits a much lower electrical conductivity than Co_3O_4 in powder form (6.4×10^{-5} mS·cm^{-1} versus 10.6 mS·cm^{-1}, respectively). This difference likely explains why $Co(CO_3)_x(OH)_y$ initially shows small capacitive currents. The capacitive current of the $Co(CO_3)_x(OH)_y$ pre-catalyst reaches a maximum at the 4th loop then decreases, whereas for Co_3O_4, it decreases continuously (Figure S11b,c), while CP steps exhibit an increase in cell voltage, suggesting progressive degradation. Consistent with previous studies,[4, 5] this degradation is likely driven by ionomer oxidation and catalyst degradation as is discussed further below. It is worth noting that those degradation modes are accelerated from repeated potential cycling leading to greater degradation compared to constant-current operation.

The superior performance of $Co(CO_3)_x(OH)_y$ at high current density may originate from its ability to sustain improved ionic conductivity to the catalyst active sites even when the ionomer is degrading via oxidation. Upon activation, $Co(CO_3)_x(OH)_y$ forms a (oxy)hydroxide surface that hosts water oxidation sites through the three-dimensional, hydrated structure. Like other metal oxides, these hydrated ionomer-free layers likely support a degree of hydroxide ion conductivity, such as found for TiO_2,[45] providing active sites spatially separated from the ionomer and thereby mitigating interfacial ionomer oxidation. Co_3O_4, however, does not undergo a substantial surface amorphization, leaving its OER sites in direct contact with the ionomer that can be degraded under oxidizing potential. This degradation limits OH^- transport to the catalyst surface, particularly at high current and oxidizing potential. For reference, a crystallographic illustration of structural hydroxyl groups in $Co(CO_3)_x(OH)_y$ is shown in Figure S12 for comparison with Co_3O_4.[46-48]

Consistent with the above hypothesis, the performance gap between $Co(CO_3)_x(OH)_y$ and Co_3O_4 anodes becomes negligible when operated in 0.10 M KOH (Figure S13). For these KOH-fed tests, no ionomer topcoat was applied so that catalyst activation was driven solely by OH^- supplied from

the electrolyte. The continuous OH^- supply also enabled faster activation of Co_3O_4, yielding comparable HFRs, R_{CT}, and kinetic parameters to $Co(CO_3)_x(OH)_y$. We also note the possibility that the activation of each of the Co-based catalysts tested here is inhomogeneous due both to the electrical resistivity of the catalyst, as well as limitations in ion transport in cases where ionomer is used with pure water.

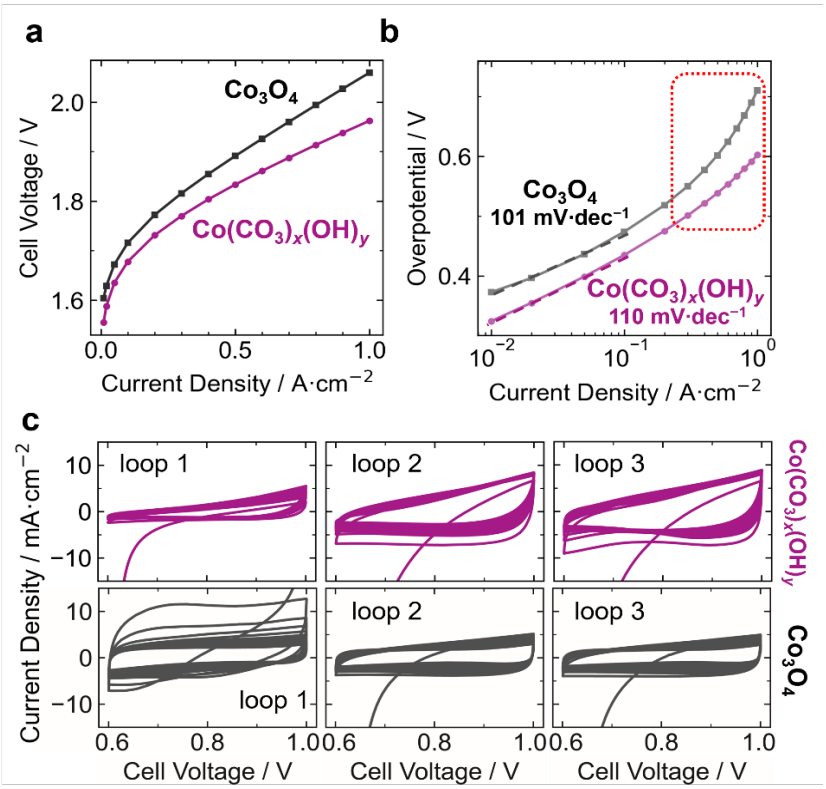

Figure 3. (a) Polarization curves of pure-water-fed AEMWE cells at 56 °C with self-supported $Co(CO_3)_x(OH)_y$ and Co_3O_4 on Ni-alloy PTLs. (b) *iR*-corrected overpotential versus current density plot of self-supported $Co(CO_3)_x(OH)_y$ and Co_3O_4 on Ni alloy PTLs. (c) CV scans devices made with anodes of $Co(CO_3)_x(OH)_y$ and Co_3O_4 on Ni alloy PTLs in pure-water-fed AEMWE cells. The data shows the initial catalyst activation. s

A durability test at 1.0 $A \cdot cm^{-2}$ was conducted for $Co(CO_3)_x(OH)_y$ and Co_3O_4 anodes in pure-water-fed AEMWE cells, with EIS and CV measurements taken before and after testing (**Figure 5** for $Co(OH)_x(CO_3)_y$ and Figure S14 for Co_3O_4). The Co_3O_4 anode shows faster voltage degradation of ~12 mV/h compared to ~8 mV/h for $Co(CO_3)_x(OH)_y$, primarily driven by increases in both HFR and R_{CT} (Figure S14b). Comparing CVs before and after the durability test, $Co(CO_3)_x(OH)_y$ retained 84% of its capacitance whereas Co_3O_4 retained 59% (Figure S14d). Post-mortem XPS analysis (Figure S15) reveals that ionomer topcoats were highly oxidized and flushed

out after 20 h of cell operation for both anodes. SEM images (Figure S16) also show that most ionomers on the anode surface were gone, and that catalyst layers underneath ionomers were also degraded, which is likely due to higher oxidative potential on the anode as ionomer continuously oxidized. However, the $Co(CO_3)_x(OH)_y$ anode retained its nanoneedle structure, while the Co_3O_4 anode showed significant catalyst layer structural breakdown. The Co_3O_4 anode exhibited a higher voltage during durability testing, suggesting that potential-driven ionomer oxidation may occur more rapidly than on $Co(CO_3)_x(OH)_y$ as well. This accelerated oxidation probably led to local pH drop at the catalyst surface under high OER current (which in the absence of OH^- to consume, generates H^+ from water), promoting the dissolution of Co species, and reducing the structural integrity of Co_3O_4 catalyst layer. *Operando* techniques, for example, X-ray absorption spectroscopy[49-60] can be valuable for confirming oxidation states of Co species and investigating the degree of reconstruction of the different cobalt-based catalysts and elucidating how this influences ionomer oxidation under operating conditions. Online inductively coupled plasma mass spectrometry studies suggest that Co dissolution stabilizes after dissolution during initial cycling or break-in, originating from surface reconstruction and volume expansion.[61, 62] Investigating Co leaching over longer operation times, when significant ionomer oxidation occurs, could help to decouple complex degradation mechanisms in AEMWE devices.

Effect of Ionomer and Supporting Electrolytes. To systematically assess the impact of ionomer on the electrochemical response and AEMWE performance, a series of self-supported $Co(CO_3)_x(OH)_y$ anodes were prepared with PiperION loadings of 0, 0.1, 0.5, 1.0, and 1.5 mg·cm^{-2}, deposited over a 1.9 mg·cm^{-2} of catalyst loading. Without an ionomer topcoat, the cell voltage was 2.31 V at 500 mA·cm^{-2} (**Figure 4a**), showing poor kinetics, high cell resistance, and a rapidly increasing voltage from 300 to 500 mA·cm^{-2}, indicating insufficient OH^- supply to the catalyst surface. Adding only 0.1 mg·cm^{-2} of ionomer improved the cell performance reaching 2.05 V at 1 A cm^{-2}, presumably from insufficient ionomer coverage to maximize the catalyst activation (Figure S6). Increasing the ionomer loading further reduced voltage, but beyond 0.5 mg·cm^{-2} additional loading (up to 1.5 mg·cm^{-2}) only resulted in a 20-mV improvement at 1.0 A·cm^{-2}. Correspondingly, HFR and R_{CT} were highest without ionomer, while those improved with increasing ionomer loading up to 0.5 mg·cm^{-2} (Figure S17 and Table S3).

To compare with the above ionomer-coated pure-water system, *ionomer-free* $Co(CO_3)_x(OH)_y$ anodes were tested in varying KOH concentrations (**Figure 4b**). Even 1.0 mM KOH improved the performance to 2.14 V, while 100 mM KOH lowered the cell voltage to 1.84 V at 1.0 $A \cdot cm^{-2}$. Consistently, performance improvement of *ionomer-free* anodes with increasing KOH concentrations was reflected in EIS data (Figure S18a and Table S4), where both HFR and R_{CT} decreased, indicating improved ionic conduction and faster charge-transfer kinetics.

For both ionomer-coated and ionomer-free anodes, we also analyzed the relationship between current densities at a low overpotential (evaluating kinetics) and capacitances. We note that the use of ionomer and pure water will focus the current density in the active regions of the porous electrode near ionomer and with electronically conductive pathways to the PTL current collector. Flooding the electrolyte with KOH will increase the ionic conductivity and tend to spread the current more evenly over the porous electrode volume, maximizing catalyst utilization. The *iR*-corrected overpotentials as a function of logarithmic current density (Tafel plots) are plotted in Figures S17b,c and S18b. *Ionomer-coated* anodes in pure water showed deviations from linearity at higher current densities, which diminished as the KOH concentration increased for *ionomer-free* anodes. This implies that KOH-fed systems better maintain OH^- supply, whereas pure-water systems rely on the ionomers to provide OH^-, likely experience a OH^- concentration gradient at the anode surface, limiting the OER performance at higher current densities. CVs (Figure S19) show increasing capacitive current with higher ionomer loading or KOH concentration, confirming that an adequate local OH^- concentration is central to increasing the number of active sites for OER.

In general, we find that higher capacitances correlate with higher kinetic current density (at η = 300 mV) as ionomer loading or KOH concentration increases (**Figure 4c**). Interestingly, at equivalent capacitances between KOH system and pure-water system, KOH-fed anodes showed much higher kinetic current densities than pure-water system. This could be due to several effects. First, the fast degradation of the ionomer directly at the catalyst surface may be unavoidable in the pure-water system, so the intrinsic activity of the ionomer-contacted OER catalyst might be impossible to measure with ionomer only. Or it may be that the intrinsic kinetics are in fact different; the cationic charge on the ionomer is all attached to the backbone of the polymer which prevents substantial conformational flexibility. The cations themselves are much larger than K^+.

Both these effects might modulate the intrinsic site-specific reaction rates for the OER and merits further study.

The activation behavior of $Co(CO_3)_x(OH)_y$ anodes was compared in AEMWE cells with dilute (0.1 mM) and more-concentrated (100 mM) KOH feeds with and without ionomer topcoats. With 0.1 mM KOH, the *ionomer-free* anode requires large voltages to activate and stabilize, showing a substantial cell-voltage gap compared to *ionomer-coated* anode during the stepwise break-in procedure (Figure S20). This behavior is expected as the limited OH^- availability hinders catalyst surface reconstruction as well as OER kinetics. Thus, the *ionomer-free* anode requires a higher cell voltage and longer time to activate while the *ionomer-coated* anode benefits from local OH^- accessibility from the ionomer and thus shows a smaller voltage decay at each current step. In contrast, in 100 mM KOH, the performance gap between *ionomer-coated* and *ionomer-free* anodes is small and the voltage stabilizes in a similar way, indicating that OH^- transport limitations are largely mitigated (Figure S20). EIS data even indicates that in concentrated KOH, the ionomer topcoat introduced additional resistance, shown by the lower HFR observed without ionomer (Figure S21e). Similarly, the capacitance increased with the presence of the ionomer topcoat under pure-water and dilute KOH conditions, but decreased in 100 mM KOH (Figures S19a and S21c,f), This results suggests that at higher KOH concentration, the ionomer layer may hinder OH^- accessibility at the catalyst surface.

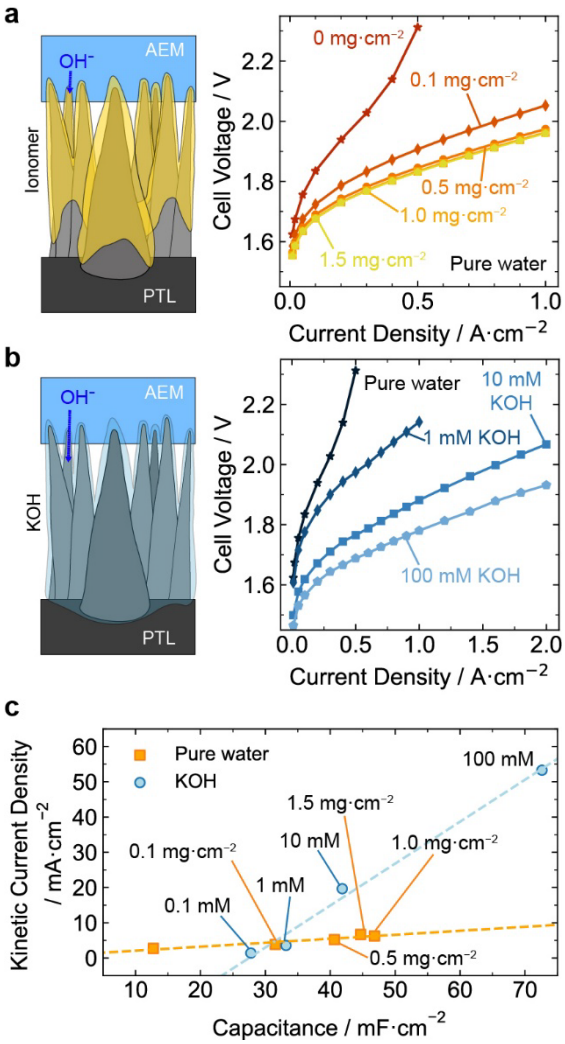

Figure. 4. (a) Scheme of *ionomer-coated* $Co(CO_3)_x(OH)_y$ anode and its polarization curves of pure-water-fed AEMWE cells at 56 °C with different PiperION ionomer topcoat loadings. (b) Scheme of *ionomer-free* $Co(CO_3)_x(OH)_y$ anode and its polarization curves of AEMWE cells at 56 °C with different concentrations of KOH feed. (c) Plot of kinetic current densities at an overpotential of 300 mV as a function of capacitance for *ionomer-coated* anodes in pure water and *ionomer-free* anodes in KOH. Dashed lines illustrate the trend but are not intended to represent a specific physical model.

With an understanding of $Co(CO_3)_x(OH)_y$ pre-catalyst activation and the effects of ionomer and KOH supporting electrolyte on the cell performance, durability tests were conducted for 1.0 $mg \cdot cm^{-2}$ ionomer-coated $Co(CO_3)_x(OH)_y$ anodes in three different systems: pure-water feed, 100 mM KOH feed, and a cell activated with 100 mM KOH then switched to pure-water feed. All cells were operated at 1.0 $A \cdot cm^{-2}$ for 20 h (**Figure 5a**), with EIS and CV measurements recorded at the beginning of life (BOL) and end of life (EOL), and some intervals (**Int I**, **Int II**), where feed mode was changed in the system. The pure-water-fed cell degraded at 8.0 $mV \cdot h^{-1}$ over the final 10 h of

the operation, while KOH feeding lowered the cell voltage by ~150 mV and stabilized (0.24 $mV \cdot h^{-1}$). In the KOH-to-pure-water system, upon flushing KOH out with pure water, the cell voltage initially increased by ~100 mV and degraded moderately at a rate of 2.7 $mV \cdot h^{-1}$. These cell performance and durability will be correlated with CVs and EIS below.

In the KOH-fed cell, a capacitance retention of 96 % between the BOL and EOL (**Figure 5b**), indicates that $Co(CO_3)_x(OH)_y$ with the reconstructed $CoO_x(OH)_y$ surface layer maintained high catalyst utilization with sufficient OH^- flux, consistent with suppression of ionomer oxidation from stabilized catalyst-ionomer interfaces by screening charge interactions at the catalyst-ionomer interface or preventing absorption.[5, 63] When the KOH was replaced with pure water, the CV at the **Int II** stage showed pseudocapacitive behavior with distinct redox features around 0.9 to 1.0 V that are only marginally enhanced relative to the pure-water BOL sample, suggesting the effective removal of KOH from the catalyst surface, along with possible charge-screening effects. Extended operation beyond 10 h did not significantly change the CV features in the KOH-to-pure-water system (compare **Int II** vs. EOL), consistent with the aforementioned moderate voltage degradation rate. The capacitances calculated at different stages are summarized in Figure S22. In contrast, the pure-water-fed system exhibited a lower initial capacitance of 43 $mF \cdot cm^{-2}$ at BOL, indicating the catalyst was not fully activated in pure water. At EOL, the capacitance decreased to 36 $mF \cdot cm^{-2}$ (84 % retention), reflecting a higher cell voltage degradation rate (8 $mV \cdot h^{-1}$). It is possible that the higher cell voltage from less-activated catalysts (pure-water only) led to accelerated ionomer oxidation, hence reducing the Co active sites.

EIS data (**Figure 5c)** is consistent with the above cell polarization and voltammetry data, showing similar EIS plots at the BOL and EOL for the KOH system, reflecting the stable cell voltage throughout operation. In contrast, R_{CT} increased from 1.050 to 1.828 $\Omega \cdot cm^2$ in the pure-water system, consistent with the fast voltage increase and degradation. When the cell operated in KOH was flushed with pure water, R_{CT} changed from 0.939 to 1.004 $\Omega \cdot cm^2$, which is not significant; however, extended operation in pure water led to further degradation in R_{CT} at EOL, reaching 1.292 $\Omega \cdot cm^2$. This suggests that although the catalyst was fully activated in KOH without substantial ionomer degradation, the limited OH^- accessibility when switching to pure-water initiated ionomer degradation at the catalyst surface. However, the increase in R_{CT} was less severe compared to the EOL analysis of the device tested in pure water only (Table S5). HFRs in all

systems decreased over 20 h, suggesting better interfacial ionic contact through ionomer/membrane from hydration or via slow membrane thinning.[64]

In the pure-water system, anodes suffered structural damage following operation, as evidenced by ionomer oxidation and catalyst degradation (Figures S15 and S16). In the KOH and KOH-to-pure-water systems, the catalyst-ionomer interface remained more stable. The SEM images (Figure S23) show that ionomer coverage was retained in both systems and XPS data (Figure S24) indicates a substantial reduction in ionomer oxidation. This stability is likely due to catalyst surface-charge-screening effect from supporting electrolytes and lower oxidizing potentials, suggesting a small degree of interfacial stabilization from the pre-treatment in KOH that may leave residual absorbed cations.

Figure 5d illustrates hypothesized molecular-level models of the anode catalyst-ionomer interfaces in different feed modes. Under oxidative potentials, $Co(OH)_x$ forms $CoO_x(OH)_y$ from oxidation of the metal centers at the catalyst surface. The degree of catalyst reconstruction appears limited to available OH^- from ionomer contacting the catalyst in the pure-water system, while mobile KOH increases the formation of $CoO_x(OH)_y$. The direct contact between the active $CoO_x(OH)_y$ and ionomer promotes electrochemical oxidation of ionomer, a dominant failure mechanism. Co-based anode catalysts with hydroxyl groups, partially deprotonated in the alkaline conditions ($pH > PZC \approx 9$),[65] can interact with the ionomer backbones or cationic groups and may also specifically absorb. However, when the cell is flooded with KOH, K^+ may adsorb at the catalyst surface, reducing absorption either via molecular or electrostatic mechanisms.[5, 63]

From this picture, we hypothesize that the improved performance and durability of the KOH-to-pure-water compared to pure-water-only cell is due to KOH-modulated activation of $Co(CO_3)_x(OH)_y$, then even after flushing KOH out with pure water, residual K^+ ions may interact with reconstructed catalyst surface, slowing ionomer oxidation and lowering the cell voltage. One might question whether the observed improvement in durability arises from catalyst pre-activation by Fe impurities present in KOH. We consider this possibility unlikely, as dynamic Fe dissolution and redeposition at the catalyst-ionomer interface are known to deteriorate the long-term stability in pure-water-fed AEMWEs.[4, 26]

The above data and analysis suggest that pre-absorption or activation in other electrolytes might be useful in exploring how to stabilize the interface. Based on, for example, hard/soft acid-base ideas,[66, 67] other ions with stronger interactions with the metal oxy(hydroxide) catalyst surface may

provide additional pathways to prevent direct interaction between the catalyst and ionomer, suppressing ionomer oxidation. The nature of catalyst-counterion interactions in the supporting electrolyte probably depends on both catalyst surface charge and the ionic charge, and radius of cations.

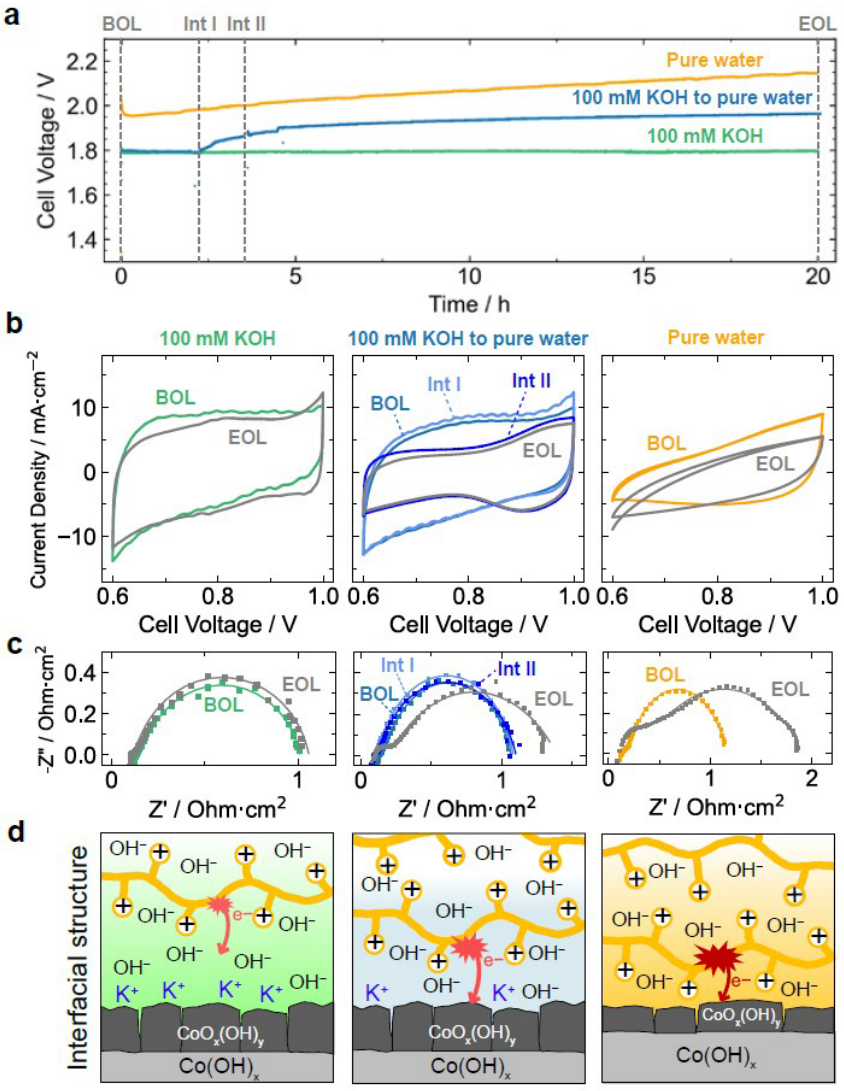

Figure 5. **Understanding degradation modes for AEMWE anodes water and KOH feed.** (a) Durability test of KOH-fed, KOH-to-pure-water-fed, and pure-water-fed AEMWE cells with PiperION coated $Co(CO_3)_x(OH)_y$ anodes. The cell was held at 1.0 A·cm^{-2} at 56 °C. During the durability test, CV and EIS were obtained at different stages. For the KOH-to-pure-water-fed system, the cell was activated in KOH for 2 h (until **Int I**) then flushed with pure water (until **Int II**). Corresponding (b) CVs at a scan rate of 100 mV·s^{-1}, and (c) EIS curves at a current density of 50 mA·cm^{-2}. (d) Molecular-level schemes of catalyst-ionomer interfaces with different feed modes at the end of life. Related processes include (*i*) the catalyst surface interacting with KOH supporting

electrolyte and/or ionomer; (*ii*) surface reconstruction of $Co(CO_3)_x(OH)_y$ to more active and conductive $CoO_x(OH)_y$ at oxidative potentials (*iii*) oxygen evolution reaction; and (*iv*) oxidation. The degree of catalyst surface reconstruction is higher with KOH feed due to mobile K^+ and OH^-. Less ionomer degradation is evident with electrolyte screening surface charge of the catalyst and physical moving ionomer further away from the catalyst surface. In the pure-water system, direct contact between active catalyst and ionomer leads to severe ionomer oxidation. In the KOH-to-pure-water system, activated $CoO_x(OH)_y$ and residual K^+ extended lifetime of the cell compared to the pure-water system.

The durability of self-supported anodes in pure-water AEMWE is limited (**Figure 5a**) due to ionomer oxidation and resulting local acidification under OER, which accelerates catalyst dissolution and mechanical breakdown. In the self-supported anode geometry, where the catalyst surface is largely covered by ionomer, facile electron transport through the catalyst layer may both lower voltage but also facilitate the ionomer degradation, in turn accelerating cell degradation. For the NP-based anode, the disconnection between catalyst nanoparticles, caused by electronically insulating ionomers covering the catalyst surface results in fewer available Co active species, and inferior performance, but somewhat lower voltage degradation rate (Figure S25).

To mitigate the degradation of self-supported anodes, a 3.5-nm thick HfO_x passivation layer was deposited by atomic-layer deposition, based on our previous work,[27] and shown to stabilize the catalyst-ionomer interface (Figure S26). While the proposed 15-h test is not sufficient to demonstrate the long-term viability of self-supported anodes with passivation coatings for commercial applications, it motivates further optimization of these coatings in robustness and ion permeability.

Conclusion

Self-supported, non-PGM Co-based anodes for AEMWE were prepared *via* a hydrothermal reaction. The self-supported Co_3O_4 anode was compared to the conventional Co_3O_4 nanoparticle ink-based anode, illustrating the importance of catalyst connectivity in device electrochemical response. We compared self-supported $Co(CO_3)_x(OH)_y$ and Co_3O_4 anodes and discovered improved performance and durability for $Co(CO_3)_x(OH)_y$ which readily converted to a more-active and water-permeated $CoO_x(OH)_y$ phase. Self-supported anodes in a pure-water-fed AEMWE with ionomer solid electrolyte had less interfacial capacitance and thus fewer accessible

active Co species than equivalent anodes with KOH supporting electrolytes. These data lead to a molecular picture whereby the systems with the best performance had a water-permeated $CoO_x(OH)_y$ phase present that is able to conduct both electrons and hydroxide. These phases have improved durability when modified with even small amounts of KOH in addition to the solid ionomer which help screen interfacial ionomer absorption and ionomer oxidation. A dedicated study of interface structure, however, is needed to fully test this hypothesis.

With these new insights into the anode catalyst structures and their interfaces with ionomer and electrolyte, we suggest methods to engineer improved self-supported anodes for pure-water-fed AEMWE systems. First, the current ionomer coating process is simple, either spray coating or dip coating to meet the desired ionomer topcoat loading. These non-optimized methods result in the ionomer coating the surface of the catalyst layer and some of the pores of the PTL. To maximize the catalyst-ionomer interface area, better methods to infiltrate ionomer through the deep pores of the catalyst coating are needed that co-optimize interface properties, ion transport, and reactant and product transport. The local pH and hydroxide-ion conductivity near the catalyst surface might also be improved with ionomers with higher ion exchange capacities (IECs),[35] for example specifically in the interface layer. The catalyst layer itself can be improved by targeting OER catalysts that have metallic conductivity, such as perovskite oxides,[68] and that can be engineered with appropriate three-dimensional structures and with controlled reconstruction of surface structures, but such metallic catalysts will likely need specific interface passivation layer development to prevent ionomer oxidation. Pre-activation or *in-situ* activation of such synthesized samples might be controlled and optimized for performance and durability by controlling the extent of oxyhydroxide formation. These more-active, electrically conductive, and morphology-engineered catalysts could then be modified with surface passivation layers, better designed to promote catalysis and hydroxide ion transport, building on the preliminary examples with the HfO_x coating demonstrated here.

Methods

Hydrothermal growth of $Co(CO_3)_x(OH)_y$ and Co_3O_4 on Ni alloy PTL. In a glass jar, 35 mmol of $Co(NO_3)_2$ hexahydrate and 7.5 mmol of urea, $CO(NH_2)_2$, were dissolved in 30 mL of 18.2 MΩ·cm high-purity water. A Ni alloy PTL substrate (Hastelloy X, Technetics Inc.) was cut in 3.3 × 3.3 cm^2, backside-masked with a 0.002-inch-thick polytetrafluoroethylene (PTFE) film and

supported by PTFE threaded rods and Nylon nuts. When the tripod-supported substrate was submerged in the solution and heated up to 100 °C in an oven, $Co(CO_3)_x(OH)_y$ grew on the PTL as well as precipitated. The hydrothermal reaction time was varied to control the loading of deposited material with 10 h found to be optimum. After hydrothermal synthesis, the sample was taken out of the jar, washed with excess pure water, and dried overnight to measure the mass loading. $Co(NO_3)_2$ hexahydrate to urea ratio was optimized as the recipe shown here. To prepare Co_3O_4 anode, the as-synthesized $Co(CO_3)_x(OH)_y$ sample was annealed at 300 °C for 2 h.

Preparation of HfO_x coating. A HfO_x coating was deposited on top of a self-supported Co_3O_4 anode using an atomic layer deposition system (Savannah, Ultratech). A HfO_x layer 3.5 nm thick was deposited from repetitive cycles of ALD deposition with 0.4 s pulses of water and 0.015 s pulses of tetrakis(dimethylamido)hafnium(IV), TDMAHf, with an interval of 5 s between each pulse at 250 °C. A Si wafer was put inside the ALD chamber along with Co_3O_4 coated Ni alloy PTL to measure the thickness of the HfO_x film using an ellipsometer.

Materials Characterization. Powder X-ray diffraction (PXRD) patterns were obtained to identify the dominant crystalline phase(s) of the prepared catalyst with a Bruker D2 Phaser benchtop diffractometer (Cu K-alpha radiation, λ=1.54 Å). Powder electrical conductivity was measured following literature procedures.[4] For example, 100 mg of catalyst powder was pressed to form a pellet, and a current-voltage curve was obtained and used to estimate the electrical conductivity of the pellet. A M-2000 spectroscopic ellipsometer (J.A. Woollam) was used to calculate HfO_x ALD film thickness on a Si wafer. The optical response from 240–1688 nm was fitted with a model of a dielectric film on a Si substrate. Scanning electron microscopy (SEM) images were obtained with a Helios Hydra (Thermo Fisher) at 5 kV using ETD or TLD mode. The anodes were cross-sectioned using a plasma focused-ion-beam (PFIB) and SEM images were obtained with elemental maps using an EDS analyzer. X-ray photoelectron spectroscopy (XPS) measurements were conducted using an ESCALAB 250 (Thermo Scientific) using an Al Kα mono-chromated source with 20 eV pass energy (500 μm spot-size). The binding energies were calibrated with the C 1s spectra (main carbon peaks at 284.8 eV). For post-mortem XPS analysis, cell operated anodes were soaked in 3 M NaCl to ion-exchange ionomer from OH^- to Cl^- form, washed with pure water vigorously and dried in air before XPS measurements.

Electrode preparation. NP-based electrodes were prepared by spray-coating ink solutions to anode and cathode PTLs. The catalyst ink solution was prepared by mixing 100 mg of nanocatalyst powder, 200 mg of 5 wt% PiperION ionomer dispersion (TP-85, Versogen), 0.5 g of 18.2 MΩ·cm high-purity water, and 1.7 g of isopropyl alcohol, corresponding to a catalyst:ionomer weight ratio of 10:1. The ionomer in the spray-coated layer is intended to prevent catalyst nanoparticle aggregation during ink preparation and spray-coating and to facilitate ionic conduction near the catalyst surface during the AEMWE cell operation. The mixed solution was sonicated for 2 h with a cooling water line immersed in the sonication bath. Pt black (Fuel Cell Store) ink solution was spray-coated on carbon paper (Toray 090, Fuel Cell Store) to prepare cathodes. Co_3O_4 (30–50 nm, US Research Nanomaterials) ink solution was spray-coated on Ni-alloy PTL as anodes. During spray-coating, the substrates were fixed on a hot plate at 80 °C to dry out solvent and form catalyst layer. After 1.5-2 $mg \cdot cm^{-2}$ of catalyst layer loading was obtained, a thin ionomer topcoat (10-20 wt% of catalyst loading, generally 0.1-0.2 $mg \cdot cm^{-2}$) was applied by spraying 2 wt% PiperION dispersion.[3, 27] For self-supported anodes after hydrothermal synthesis, PiperION topcoats were applied by dipping the anode into 2 wt% PiperION dispersion with the catalyst-coated sides facing down. After dipping, the samples were placed on the hot plate at 80 °C to remove solvent. The dipping-and-drying step was repeated until the target ionomer loading was obtained with a typical loading of 1 $mg \cdot cm^{-2}$. The loading of ionomer topcoat was calculated from the mass difference of anodes before and after dip-coating. Ionomer-free anodes were tested in the electrolyzer without this dip-coating procedure.

Membrane electrode assembly (MEA) fabrication and AEMWE single cell operation. The AEMWE single cell assembly was adopted from literature.[3, 27] A preconditioned AEM (40 μm PiperION, Versogen) was sandwiched between 1.0 cm^2 precut cathode and anode electrodes with gaskets. The MEA was compressed in flow fields and bipolar plates. 18.2 MΩ·cm high-purity water was supplied to both anode and cathode from a water tank at 60 $mL \cdot m^{-1}$. The cell temperature was set to 56 ± 1 °C with the water tank (15 L) at 62 °C. KOH electrolyte was prepared by dissolving KOH pellets (Thermo Scientific Chemicals, 85%) dissolved in DI water without additional purification steps. Thus, trace Fe impurities were present. Different concentrations of KOH prepared in the KOH tank (6L) were fed to both anode and cathode for KOH concentration-dependent performance measurements.

The electrolyzer test was conducted with a BioLogic VSP-300 potentiostat equipped with a 10 A/5 V booster. Starting from 100 $mA \cdot cm^{-2}$, the current applied to the cell was stepped up to 1.0 $A \cdot cm^{-2}$ with an interval of 100 $mA \cdot cm^{-2}$ as a cell break-in procedure. The current was held for 2 min for each current step. After breaking in the cell, the current was stepped down with an interval of 100 $mA \cdot cm^{-2}$, held for 10 s for each step, back to 100 $mA \cdot cm^{-2}$ with two additional current steps to 50 and 10 $mA \cdot cm^{-2}$ to obtain a polarization curve. Electrochemical impedance was measured at 50 $mA \cdot cm^{-2}$ with a frequency range of 1 MHz to 100 mHz. Cyclic voltammograms were obtained by sweeping a cell voltage between 0.6 V and 1.0 V with a scan rate of 100 $mV \cdot s^{-1}$, which is sufficiently fast to observe limitations of electron and OH^- transport affecting the measured number of electroactive sites. The capacitances were determined by averaging charges over the sweeping potential range during a CV scan. For durability tests, the cell was held at either 500 $mA \cdot cm^{-2}$ or 1.0 $A \cdot cm^{-2}$ for a certain period. EIS and CV measurements were repeated after the durability test. When the cell was operated with KOH feed, the current was held up to 2.0 $A \cdot cm^{-2}$ for the initial cell break-in and obtaining polarization curve. To monitor the activation and degradation of $Co(OH)_x(CO_3)_y$ and Co_3O_4 anodes, the cell was cycled with a voltage range of 0.6 V to 1.0 V 50 times (CVs) then a constant current of 0.5 $A \cdot cm^{-2}$ was applied for 10 min (CP). The CV and CP steps were repeated 20 times in a loop. For durability comparison with different feed modes, EIS and CV were obtained before and after operating at 1.0 $A \cdot cm^{-2}$. For the KOH-to-pure-water system, the cell was initially operated with 100 mM KOH feed for 2 h, and EIS and CV collected to monitor the initial catalyst activation (**Int I**). Subsequently, the cell was flushed with > 4 L of pure water to remove the KOH (with the exception perhaps of strongly absorbed species) then the operation continued for an additional hour with the cell connected and recirculated with a large pure water reservoir (~15 L). After these steps, the durability test was interrupted to obtain another set of EIS and CV (**Int II**) to assess how the activated catalyst changed upon transitioning to the pure-water system.

Author Information

Corresponding Author

Shannon W. Boettcher - *Departments of Chemical & Biomolecular Engineering and Chemistry, University of California, Berkeley, CA 94720, United States; Energy Storage and Distributed Resources Division, Lawrence Berkeley National Laboratory, Berkeley, CA 94720, United States;*

Oregon Center for Electrochemistry, Department of Chemistry and Biochemistry, University of Oregon, Eugene, OR 97403, United States. boettcher@berkeley.edu

Authors

Minkyoung Kwak - *Oregon Center for Electrochemistry, Department of Chemistry and Biochemistry, University of Oregon, Eugene, OR 97403, United States; Departments of Chemical & Biomolecular Engineering and Chemistry, University of California, Berkeley, CA 94720, United States; Energy Storage and Distributed Resources Division, Lawrence Berkeley National Laboratory, Berkeley, CA 94720, United States.*

Shujin Hou - *Departments of Chemical & Biomolecular Engineering and Chemistry, University of California, Berkeley, CA 94720, United States; Energy Storage and Distributed Resources Division, Lawrence Berkeley National Laboratory, Berkeley, CA 94720, United States.*

Kieran J. Spence - *De Nora Tech, LLC, Concord, OH 44077, United States.*

Tekalign T. Debela - *Oregon Center for Electrochemistry, Department of Chemistry and Biochemistry, University of Oregon, Eugene, OR 97403, United States; Department of Chemistry and Physical Science, Methodist University, Fayetteville, NC 28311, United States.*

Notes

K.J.S. is an employee of De Nora Tech, which produces commercial electrodes for water electrolyzers.

Author contributions

M.K. and S.W.B. conceptualized and led the project. M.K. prepared samples, collected electrolyzer data, and characterized samples. S.H. and K.J.S. provided feedback on the experiments and data analysis. T.T.D. provided crystallographic information files. M.K. and S.W.B. wrote the original draft and all authors reviewed and edited the manuscript.

Supporting Information

The Supporting Information is available free of charge.

Optimization of hydrothermal synthesis; additional materials characterization data, including SEM images and XP spectra; implications for interpretation and analysis of EIS and CV data; and AEMWE single cell polarization curves

Acknowledgements

The catalyst science and development work was supported by the National Science Foundation, Chemical Catalysis Program award #2400195. The electrolyzer device work was supported by De Nora Tech, LLC and the US Department of Energy (DOE), Office of Energy Efficiency and Renewable Energy, award DE-EE0011322. We acknowledge the use of shared instrumentation in the Center for Advanced Materials Characterization in Oregon (CAMCOR). M.K. thanks Dr. Paul Kempler and Dr. Arunavo Chakraborty for insightful discussions. We acknowledge that this work is adapted in part from M.K.'s doctoral dissertation, which is available through ProQuest (No. 31998334).[69]

Reference

(1) Lee, S. A.; Kim, J.; Kwon, K. C.; Park, S. H.; Jang, H. W. Anion Exchange Membrane Water Electrolysis for Sustainable Large-Scale Hydrogen Production. *Carbon Neutralization* **2022**, *1* (1), 26-48. DOI: 10.1002/cnl2.9.

(2) Li, D.; Motz, A. R.; Bae, C.; Fujimoto, C.; Yang, G.; Zhang, F. Y.; Ayers, K. E.; Kim, Y. S. Durability of Anion Exchange Membrane Water Electrolyzers. *Energy Environ. Sci.* **2021**, *14* (6), 3393-3419. DOI: 10.1039/d0ee04086j.

(3) Lindquist, G. A.; Oener, S. Z.; Krivina, R.; Motz, A. R.; Keane, A.; Capuano, C.; Ayers, K. E.; Boettcher, S. W. Performance and Durability of Pure-Water-Fed Anion Exchange Membrane Electrolyzers Using Baseline Materials and Operation. *ACS Applied Materials and Interfaces* **2021**, *13* (44), 51917-51924. DOI: 10.1021/acsami.1c06053.

(4) Krivina, R. A.; Lindquist, G. A.; Beaudoin, S. R.; Stovall, T. N.; Thompson, W. L.; Twight, L. P.; Marsh, D.; Grzyb, J.; Fabrizio, K.; Hutchison, J. E.; et al. Anode Catalysts in Anion-Exchange-Membrane Electrolysis without Supporting Electrolyte: Conductivity, Dynamics, and Ionomer Degradation. *Adv. Mater.* **2022**, *34* (35). DOI: 10.1002/adma.202203033.

(5) Lindquist, G. A.; Gaitor, J. C.; Thompson, W. L.; Brogden, V.; Noonan, K. J. T.; Boettcher, S. W. Oxidative Instability of Ionomers in Hydroxide-Exchange-Membrane Water Electrolyzers. *Energy Environ. Sci.* **2023**, *16*, 4373-4387. DOI: 10.1039/D3EE01293J.

(6) Möckl, M.; Ernst, M., F.; Kornherr, M.; Allebrod, F.; Bernt, M.; Byrknes, J.; Eickes, C.; Gebauer, C.; Moskovtseva, A.; Gasteiger, H., A. Durability Testing of Low-Iridium PEM Water Electrolysis Membrane Electrode Assemblies. *J. Electrochem. Soc.* **2022**, *169* (6), 064505. DOI: 10.1149/1945-7111/ac6d14.

(7) Mark, C.; Christopher, M. Z.; Margery, R. Perspectives on Current and Future Iridium Demand and Iridium Oxide Catalysts for PEM Water Electrolysis. *Catal. Today* **2023**, *420*, 114140. DOI: 10.1016/j.cattod.2023.114140.

(8) Carmo, M.; Fritz, D. L.; Mergel, J.; Stolten, D. A Comprehensive Review on PEM Water Electrolysis. *Int. J. Hydrogen Energy* **2013**, *38* (12), 4901-4934. DOI: 10.1016/j.ijhydene.2013.01.151.
(9) Scarpelli, F.; Godbert, N.; Crispini, A.; Aiello, I. Nanostructured Iridium Oxide: State of the Art. *Inorganics* **2022**, *10* (8), 115. DOI: 10.3390/inorganics10080115.
(10) Christine, M.; Michel, S.; Boris, B.; Richard, H.-R. Is Iridium Demand a Potential Bottleneck in the Realization of Large-Scale PEM Water Electrolysis? *Int. J. Hydrogen Energy* **2021**, *46* (46), 23581-23590. DOI: 10.1016/j.ijhydene.2021.04.174.
(11) Juchan, Y.; Myeong Je, J.; Xiaojun, Z.; Yoo Sei, P.; Jooyoung, L.; Sung Mook, C.; Yadong, Y. Non-Precious Electrocatalysts for Oxygen Evolution Reaction in Anion Exchange Membrane Water Electrolysis: A Mini Review. *Electrochem. Commun.* **2021**, *131*, 107118. DOI: 10.1016/j.elecom.2021.107118.
(12) Jang, M. J.; Yang, J.; Lee, J.; Park, Y. S.; Jeong, J.; Park, S. M.; Jeong, J.-Y.; Yin, Y.; Seo, M.-H.; Choi, S. M.; et al. Superior Performance and Stability of Anion Exchange Membrane Water Electrolysis: pH-Controlled Copper Cobalt Oxide Nanoparticles for the Oxygen Evolution Reaction. *J. Mater. Chem. A* **2020**, *8* (8), 4290-4299. DOI: 10.1039/C9TA13137J.
(13) Trotochaud, L.; Ranney, J. K.; Williams, K. N.; Boettcher, S. W. Solution-Cast Metal Oxide Thin Film Electrocatalysts for Oxygen Evolution. *J. Am. Chem. Soc.* **2012**, *134* (41), 17253-17261. DOI: 10.1021/ja307507a.
(14) Volk, E. K.; Kreider, M. E.; Kwon, S.; Alia, S. M. Recent Progress in Understanding the Catalyst Layer in Anion Exchange Membrane Electrolyzers – Durability, Utilization, and Integration. *EES Catalysis* **2024**, *2* (1), 109-137. DOI: 10.1039/D3EY00193H.
(15) Janghoon, P.; Zhenye, K.; Guido, B.; Michael, U.; Scott, A. M. Roll-to-roll Production of Catalyst Coated Membranes for Low-Temperature Electrolyzers. *J. Power Sources* **2020**, *479*, 228819. DOI: 10.1016/j.jpowsour.2020.228819.
(16) Yang, H.; Driess, M.; Menezes, P. W. Self-Supported Electrocatalysts for Practical Water Electrolysis. *Adv. Energy Mater.* **2021**, *11* (39), 2102074. DOI: 10.1002/aenm.202102074.
(17) Sun, H.; Yan, Z.; Liu, F.; Xu, W.; Cheng, F.; Chen, J. Self-Supported Transition-Metal-Based Electrocatalysts for Hydrogen and Oxygen Evolution. *Adv. Mater.* **2020**, *32* (3), 1806326. DOI: 10.1002/adma.201806326.
(18) Romiluyi, O.; Danilovic, N.; Bell, A. T.; Weber, A. Z. Membrane-Electrode Assembly Design Parameters for Optimal CO_2 Reduction. *Electrochemical Science Advances* **2023**, *3* (1), e2100186. DOI: 10.1002/elsa.202100186.
(19) Krivina, R. A.; Lindquist, G. A.; Yang, M. C.; Cook, A. K.; Hendon, C. H.; Motz, A. R.; Capuano, C.; Ayers, K. E.; Hutchison, J. E.; Boettcher, S. W. Three-Electrode Study of Electrochemical Ionomer Degradation Relevant to Anion-Exchange-Membrane Water Electrolyzers. *ACS Applied Materials and Interfaces* **2022**, *14* (16), 18261-18274. DOI: 10.1021/acsami.1c22472.
(20) Wang, P.; Wang, B. Designing Self-Supported Electrocatalysts for Electrochemical Water Splitting: Surface/Interface Engineering toward Enhanced Electrocatalytic Performance. *ACS Appl. Mater. Interfaces* **2021**, *13* (50), 59593-59617. DOI: 10.1021/acsami.1c17448.
(21) Qiucheng, X.; Liyue, Z.; Jiahao, Z.; Jingyu, W.; Yanjie, H.; Hao, J.; Chunzhong, L. Anion Exchange Membrane Water Electrolyzer: Electrode Design, Lab-Scaled Testing System and Performance Evaluation. *EnergyChem* **2022**, *4* (5), 100087. DOI: 10.1016/j.enchem.2022.100087.
(22) Lei, W.; Ziang, X.; Peican, W.; Peng-Fei, L.; Qin, X.; Baoguo, W. Dual Regulation Both Intrinsic Activity and Mass Transport for Self-Supported Electrodes Using in Anion Exchange Membrane Water Electrolysis. *Chemical Engineering Journal* **2022**, *431*, 133942. DOI: 10.1016/j.cej.2021.133942.
(23) Zheng, Y.; Serban, A.; Zhang, H.; Chen, N.; Song, F.; Hu, X. Anion Exchange Ionomers Enable Sustained Pure-Water Electrolysis Using Platinum-Group-Metal-Free Electrocatalysts. *ACS Energy Lett.* **2023**, 5018-5024. DOI: 10.1021/acsenergylett.3c01866.

(24) Kong, T.-H.; Thangavel, P.; Shin, S.; Kwon, S.; Choi, H.; Lee, H.; Park, N.; Woo, J.-J.; Kwon, Y. In-Situ Ionomer-Free Catalyst-Coated Membranes for Anion Exchange Membrane Water Electrolyzers. *ACS Energy Lett.* **2023**, *8* (11), 4666-4673. DOI: 10.1021/acsenergylett.3c01418.
(25) Lindquist, G. A.; Boettcher, S. W. Reports From The Frontier: Overcoming Limitations for Pure-water Anion-exchange-membrane Electrolysis. *Electrochem. Soc. Interface* **2023**, *32* (2), 32. DOI: 10.1149/2.F05232IF.
(26) Zhang, L.; Xu, Q.; Hu, Y.; Chen, L.; Jiang, H. Benchmarking the pH–Stability Relationship of Metal Oxide Anodes in Anion Exchange Membrane Water Electrolysis. *ACS Sustainable Chemistry & Engineering* **2023**, *11* (36), 13251-13259. DOI: 10.1021/acssuschemeng.3c01619.
(27) Kwak, M.; Ojha, K.; Shen, M.; Boettcher, S. W. Electrically Insulated Catalyst–Ionomer Anode Interfaces toward Durable Alkaline Membrane Electrolyzers. *ACS Energy Lett.* **2024**, *9* (3), 1025-1034. DOI: 10.1021/acsenergylett.3c02620.
(28) Rong, C.; Hsin-Yi, W.; Jianwei, M.; Hongbin, Y.; Bin, L. A Flexible High-Performance Oxygen Evolution Electrode with Three-Dimensional $NiCo_2O_4$ Core-Shell Nanowires. *Nano Energy* **2015**, *11*, 333-340. DOI: 10.1016/j.nanoen.2014.11.021.
(29) Ji, H.; Ma, Y.; Cai, Z.; Yun, M.; Han, J.; Tong, Z.; Wang, M.; Suhr, J.; Xiao, L.; Jia, S.; et al. Mesoporous Cobalt Oxide (CoO_x) Nanowires with Different Aspect Ratios for High Performance Hybrid Supercapacitors. *Nanomaterials (Basel, Switzerland)* **2023**, *13* (4). DOI: 10.3390/nano13040749.
(30) Yang, Q.; Lu, Z.; Sun, X.; Liu, J. Ultrathin Co_3O_4 Nanosheet Arrays with High Supercapacitive Performance. *Sci. Rep.* **2013**, *3* (1), 3537. DOI: 10.1038/srep03537.
(31) Li, X.; Kale, G. M. Urea-Based Hydrothermal Synthesis of ITO Nanopowders. *J. Phys. Conf. Ser.* **2006**, *26* (1), 319. DOI: 10.1088/1742-6596/26/1/077.
(32) Mark, C. B.; Brad, P. P.; Andrew, P. G.; Leo, W. M. L.; Andrea, R. G.; Roger St, C. S. Resolving Surface Chemical States in XPS Analysis of First Row Transition Metals, Oxides and Hydroxides: Cr, Mn, Fe, Co and Ni. *Appl. Surf. Sci.* **2011**, *257* (7), 2717-2730. DOI: 10.1016/j.apsusc.2010.10.051.
(33) Chen, H.; Falling, L. J.; Kersell, H.; Yan, G.; Zhao, X.; Oliver-Meseguer, J.; Jaugstetter, M.; Nemsak, S.; Hunt, A.; Waluyo, I.; et al. Elucidating the Active Phases of CoO_x Films on Au(111) in the CO Oxidation Reaction. *Nat. Commun.* **2023**, *14* (1), 6889. DOI: 10.1038/s41467-023-42301-7.
(34) Stoch, J.; Gablankowska-Kukucz, J. The Effect of Carbonate Contaminations on the XPS O 1s Band Structure in Metal Oxides. *Surf. Interface Anal.* **1991**, *17* (3), 165-167. DOI: 10.1002/sia.740170308.
(35) Xiao, J.; Oliveira, A. M.; Wang, L.; Zhao, Y.; Wang, T.; Wang, J.; Setzler, B. P.; Yan, Y. Water-Fed Hydroxide Exchange Membrane Electrolyzer Enabled by a Fluoride-Incorporated Nickel–Iron Oxyhydroxide Oxygen Evolution Electrode. *ACS Catal.* **2021**, *11* (1), 264-270. DOI: 10.1021/acscatal.0c04200.
(36) Yongzhen, Q.; Jiangjin, L.; Dinesh, C. S.; Ying, H.; Andrea, P.; Andrew, T. H.; Iryna, V. Z. Interpreting Ionic Conductivity for Polymer Electrolyte Fuel Cell Catalyst Layers with Electrochemical Impedance Spectroscopy and Transmission Line Modeling. *J. Electrochem. Soc.* **2021**, *168* (5), 054502. DOI: 10.1149/1945-7111/abf96d.
(37) Emily, K. V.; Stephanie, K.; Shaun, M. A. Catalytic Activity and Stability of Non-Platinum Group Metal Oxides for the Oxygen Evolution Reaction in Anion Exchange Membrane Electrolyzers. *J. Electrochem. Soc.* **2023**, *170* (6), 064506. DOI: 10.1149/1945-7111/acd605.
(38) Wagh, K. S.; Mane, S. M.; Teli, A. M.; Shin, J. C.; Lee, J. Recent Advancements in Co_3O_4-Based Composites for Enhanced Electrocatalytic Water Splitting. *Micromachines* **2024**, *15* (12), 1450. DOI: 10.3390/mi15121450.
(39) Burke, M. S.; Zou, S.; Enman, L. J.; Kellon, J. E.; Gabor, C. A.; Pledger, E.; Boettcher, S. W. Revised Oxygen Evolution Reaction Activity Trends for First-Row Transition-Metal (Oxy)hydroxides in Alkaline Media. *J. Phys. Chem. Lett.* **2015**, *6* (18), 3737-3742. DOI: 10.1021/acs.jpclett.5b01650.

(40) Kreider, M. E.; Yu, H.; Osmieri, L.; Parimuha, M. R.; Reeves, K. S.; Marin, D. H.; Hannagan, R. T.; Volk, E. K.; Jaramillo, T. F.; Young, J. L.; et al. Understanding the Effects of Anode Catalyst Conductivity and Loading on Catalyst Layer Utilization and Performance for Anion Exchange Membrane Water Electrolysis. *ACS Catal.* **2024**, *14* (14), 10806-10819. DOI: 10.1021/acscatal.4c02932.
(41) Yang, J.; Liu, H.; Martens, W. N.; Frost, R. L. Synthesis and Characterization of Cobalt Hydroxide, Cobalt Oxyhydroxide, and Cobalt Oxide Nanodiscs. *J. Phys. Chem. C* **2010**, *114* (1), 111-119. DOI: 10.1021/jp908548f.
(42) Pralong, V.; Delahaye-Vidal, A.; Beaudoin, B.; Gérand, B.; Tarascon, J. M. Oxidation Mechanism of Cobalt Hydroxide to Cobalt Oxyhydroxide. *J. Mater. Chem.* **1999**, *9* (4), 955-960. DOI: 10.1039/A807689H.
(43) Padgett, E.; Bender, G.; Haug, A.; Lewinski, K.; Sun, F.; Yu, H.; Cullen, D. A.; Steinbach, A. J.; Alia, S. M. Catalyst Layer Resistance and Utilization in PEM Electrolysis. *J. Electrochem. Soc.* **2023**, *170* (8), 084512. DOI: 10.1149/1945-7111/acee25.
(44) Hassan, N. U.; Zheng, Y.; Kohl, P. A.; Mustain, W. E. KOH vs Deionized Water Operation in Anion Exchange Membrane Electrolyzers. *J. Electrochem. Soc.* **2022**, *169* (4), 044526. DOI: 10.1149/1945-7111/ac5f1d.
(45) Chen, L.; Xu, Q.; Oener, S. Z.; Fabrizio, K.; Boettcher, S. W. Design Principles for Water Dissociation Catalysts in High-Performance Bipolar Membranes. *Nat. Commun.* **2022**, *13* (1), 3846. DOI: 10.1038/s41467-022-31429-7.
(46) Oqmhula, K.; Toma, T.; Maezono, R.; Hongo, K. First-Principles-Based Insight into Electrochemical Reactivity in a Cobalt-Carbonate-Hydroxide Pseudocapacitor. *ACS Omega* **2023**, *8* (7), 6743-6752. DOI: 10.1021/acsomega.2c07362.
(47) Bhojane, P.; Le Bail, A.; Shirage, P. M. A Quarter of a Century After Its Synthesis and with >200 Papers Based on Its Use, '$Co(CO_3)_{0.5}(OH)\cdot 0.11H_2O$' Proves to be $Co_6(CO_3)_2(OH)_8\cdot H_2O$ from Synchrotron Powder Diffraction Data. *Acta Crystallographica Section C* **2019**, *75* (1), 61-64. DOI: 10.1107/S2053229618017734.
(48) Momma, K.; Izumi, F. VESTA 3 for Three-Dimensional Visualization of Crystal, Volumetric and Morphology Data. *J. Appl. Crystallogr.* **2011**, *44* (6), 1272-1276. DOI: 10.1107/S0021889811038970.
(49) Huang, J.; Zhang, Z.; Spezzati, C.; Clark, A. H.; Hales, N.; Genz, N. S.; Daffé, N.; Skoupy, R.; Gubler, L.; Castelli, I. E.; et al. Directly Synthesized Cobalt Oxyhydroxide as an Oxygen Evolution Catalyst in Proton Exchange Membrane Water Electrolyzers. *Nat. Commun.* **2025**, *16* (1), 7518. DOI: 10.1038/s41467-025-62744-4.
(50) Huang, J.; Clark, A. H.; Hales, N.; Crossley, K.; Guehl, J.; Skoupy, R.; Schmidt, T. J.; Fabbri, E. Oxidation of Interfacial Cobalt Controls the pH Dependence of the Oxygen Evolution Reaction. *Nat. Chem.* **2025**, *17* (6), 856-864. DOI: 10.1038/s41557-025-01784-1.
(51) Bergmann, A.; Martinez-Moreno, E.; Teschner, D.; Chernev, P.; Gliech, M.; de Araújo, J. F.; Reier, T.; Dau, H.; Strasser, P. Reversible amorphization and the catalytically active state of crystalline Co3O4 during oxygen evolution. *Nat. Commun.* **2015**, *6* (1), 8625. DOI: 10.1038/ncomms9625.
(52) Shengmei, C.; Longtao, M.; Zhaodong, H.; Guojin, L.; Chunyi, Z. In Situ/Operando Analysis of Surface Reconstruction of Transition Metal-based Oxygen Evolution Electrocatalysts. *Cell Reports Physical Science* **2022**, *3* (1), 100729. DOI: 10.1016/j.xcrp.2021.100729.
(53) Enman, L. J.; Stevens, M. B.; Dahan, M. H.; Nellist, M. R.; Toroker, M. C.; Boettcher, S. W. Operando X-Ray Absorption Spectroscopy Shows Iron Oxidation Is Concurrent with Oxygen Evolution in Cobalt–Iron (Oxy)hydroxide Electrocatalysts. *Angew. Chem. Int. Ed.* **2018**, *57* (39), 12840-12844. DOI: 10.1002/anie.201808818.
(54) Kreider, M. E.; Burke Stevens, M. Material Changes in Electrocatalysis: An In Situ/Operando Focus on the Dynamics of Cobalt-Based Oxygen Reduction and Evolution Catalysts. *ChemElectroChem* **2023**, *10* (3), e202200958. DOI: 10.1002/celc.202200958.

(55) Bergmann, A.; Jones, T. E.; Martinez Moreno, E.; Teschner, D.; Chernev, P.; Gliech, M.; Reier, T.; Dau, H.; Strasser, P. Unified Structural Motifs of the Catalytically Active State of Co(oxyhydr)oxides during the Electrochemical Oxygen Evolution Reaction. *Nat. Catal.* **2018**, *1* (9), 711-719. DOI: 10.1038/s41929-018-0141-2.
(56) Ou, Y.; Twight, L. P.; Samanta, B.; Liu, L.; Biswas, S.; Fehrs, J. L.; Sagui, N. A.; Villalobos, J.; Morales-Santelices, J.; Antipin, D.; et al. Cooperative Fe Sites on Transition Metal (Oxy)Hydroxides Drive High Oxygen Evolution Activity in Base. *Nat. Commun.* **2023**, *14* (1), 7688. DOI: 10.1038/s41467-023-43305-z.
(57) Liu, L.; Twight, L. P.; Xi, S.; Ou, Y.; Boettcher, S. W. Dynamics of Fe Adsorption and Desorption from CoO_xH_y During Oxygen Evolution Reaction Electrocatalysis. *ACS Catal.* **2025**, *15* (1), 275-283. DOI: 10.1021/acscatal.4c04777.
(58) Krivina, R. A.; Ou, Y.; Xu, Q.; Twight, L. P.; Stovall, T. N.; Boettcher, S. W. Oxygen Electrocatalysis on Mixed-Metal Oxides/Oxyhydroxides: From Fundamentals to Membrane Electrolyzer Technology. *Accounts of Materials Research* **2021**, *2* (7), 548-558. DOI: 10.1021/accountsmr.1c00087.
(59) Lee, W. H.; Han, M. H.; Ko, Y.-J.; Min, B. K.; Chae, K. H.; Oh, H.-S. Electrode Reconstruction Strategy for Oxygen Evolution Reaction: Maintaining Fe-CoOOH Phase with Intermediate-Spin State during Electrolysis. *Nat. Commun.* **2022**, *13* (1), 605. DOI: 10.1038/s41467-022-28260-5.
(60) Cabrera-German, D.; Gomez-Sosa, G.; Herrera-Gomez, A. Accurate peak Fitting and Subsequent Quantitative Composition Analysis of the Spectrum of Co 2p Obtained with Al Kα Radiation: I: Cobalt Spinel. *Surf. Interface Anal.* **2016**, *48* (5), 252-256. DOI: 10.1002/sia.5933.
(61) Priamushko, T.; Franz, E.; Logar, A.; Bijelić, L.; Guggenberger, P.; Escalera-López, D.; Zlatar, M.; Libuda, J.; Kleitz, F.; Hodnik, N.; et al. Be Aware of Transient Dissolution Processes in Co3O4 Acidic Oxygen Evolution Reaction Electrocatalysts. *J. Am. Chem. Soc.* **2025**, *147* (4), 3517-3528. DOI: 10.1021/jacs.4c14952.
(62) Hou, S.; Sekar, A.; Zhao, Y.; Kwak, M.; Oh, J.; Li, K. K.-Y.; Wu, P.; Hannagan, R. T.; Cartagena, V.; Ekennia, A. C.; et al. Durable, pure water–fed, anion-exchange membrane electrolyzers through interphase engineering. *Science* **2025**, *390* (6770), 294-298. DOI: doi:10.1126/science.adw7100.
(63) Lim, J.; Klein, J. M.; Lee, S. G.; Park, E. J.; Kang, S. Y.; Maurya, S.; Mustain, W. E.; Boettcher, S.; Kim, Y. S. Addressing the Challenge of Electrochemical Ionomer Oxidation in Future Anion Exchange Membrane Water Electrolyzers. *ACS Energy Lett.* **2024**, *9* (6), 3074-3083. DOI: 10.1021/acsenergylett.4c00832.
(64) Malone, I.; Ünsal, S.; Young, R. S.; Jones, M. P.; Spanu, F.; Marathe, S.; Jervis, R.; Hamilton, H. G. C.; Zalitis, C. M.; Miller, T. S.; et al. Deconvoluting Degradation Mechanisms in Anion Exchange Membrane Water Electrolysis Using Operando X-ray Microtomography. *Adv. Energy Mater.*, e202501339 (*in press*). DOI: 10.1002/aenm.202501339.
(65) Ardizzone, S.; Spinolo, G.; Trasatti, S. The Point of Zero Charge of Co_3O_4 Prepared by Thermal Decomposition of Basic Cobalt Carbonate. *Electrochim. Acta* **1995**, *40* (16), 2683-2686. DOI: 10.1016/0013-4686(95)00238-A.
(66) Pearson, R. G. Absolute Electronegativity and Hardness: Application to Inorganic Chemistry. *Inorg. Chem.* **1988**, *27* (4), 734-740. DOI: 10.1021/ic00277a030.
(67) Birkel, A.; Loges, N.; Mugnaioli, E.; Branscheid, R.; Koll, D.; Frank, S.; Panthfer, M.; Tremel, W. Interaction of Alkaline Metal Cations with Oxidic Surfaces: Effect on the Morphology of SnO_2 Nanoparticles. *Langmuir* **2010**, *26* (5), 3590-3595. DOI: 10.1021/la902994r.
(68) Zhai, T.; Wang, H.; Beaudoin, S. R.; Zhang, R.; Kwak, M.; Hou, S.; Guo, Z.; Boettcher, S. W. Perovskite Catalysts for Pure-Water-Fed Anion-Exchange-Membrane Electrolyzer Anodes: Co-design of Electrically Conductive Nanoparticle Cores and Active Surfaces. *J. Am. Chem. Soc.* **2025**, *147* (18), 15448-15458. DOI: 10.1021/jacs.5c01621.

(69) Kwak, M. Design of Anode Catalyst-Ionomer Interfaces for Durable Anion-Exchange-Membrane Water Electrolyzers. *Ph.D. Dissertation, University of Oregon, Eugene, OR* **2025**; ProQuest No. 31998334.

Table of Contents Graphic

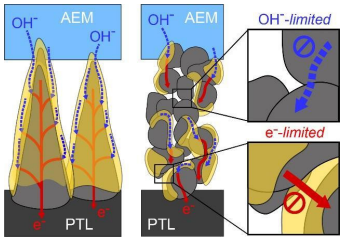

The self-supported Co-based anodes were developed as opposed to nanoparticle ink-based anodes, highlighting the importance of continuous electron and ion transport pathways.